Electronic Supporting Information for: A Dramatic Reduction in the Sintering Temperature of the Refractory Sodium β''-Alumina Solid Electrolyte via Cold Sintering

Zane Grady*[,1,2] , Arnaud Ndayishimiye[2], Clive Randall[1,2]

[1]Materials Science and Engineering Department, The Pennsylvania State University, University Park, PA, 16802

[2]Materials Research Institute, Millennium Science Complex, University Park, PA, 16802

*Corresponding author: zmg19@psu.edu, tel.: (401)741-3432

1. Cold Sintering

A detailed description of the cold sintering process is provided alongside a schematic (**Figure S1, Figure S2A**). First, SBA powder is removed from the vacuum oven and weighed in an appropriate ratio relative to the solid sodium hydroxide powder (ca. 10 wt.% hydroxide to 90 wt.% SBA). The two powders are then mixed by hand in a fume hood to obtain a homogenous dispersion (ca. 5 minutes). The powder mixture is then charged into the cylindrical stainless steel pressing die (inner diameter = 13 mm), separated from the punch faces by a nickel foil (Alfa Aesar, 0.05 in). The die is then fitted into a mica band heater and placed inside a Carver press. A pressure of 350 MPa is applied, and the heating elements are engaged to the desired temperature. The platens of the Carver press are simultaneously heated to ca. 275°C to reduce thermal losses. Upon reaching the prescribed hold time, all heating elements are turned off, but the pressure remains applied while a 6-inch fan is employed to cool the system. During cooling, the pressure is released slowly owing to the cooling of the hydraulic oil used to maintain the uniaxial pressure. A schematic representation of the pressure and temperature as a function of time are given in **Figure S2B**. After about 1 hour of cooling, the die is removed from the press and the cold sintered pellet is ejected.

It is possible to monitor densification as a function of time during the cold sintering process by employing a dilatometer between the platens of the Carver press, as described by previous authors (**Figure S2A**).[1], [2] However,

the Carver press equipped with the dilatometer is limited to cold sintering temperatures below ca. 275°C, so the *in-situ* cold sintering of SBA experiment was carried out using a low temperature KOH/NaOH eutectic salt mixture at 200°C rather than the pure NaOH used for the rest of the study.[3], [4] Despite this lower temperature, a pellet of high density is obtained (93%) and the evolution of the density with time can be clearly observed (**Figure S2C-D**). While high density is achieved, SBA pellets densified with a eutectic mixture of NaOH/KOH have a low ionic conductivity owing to K^+/Na^+ ion-exchange, which results in a detrimental mixed alkali effect on the total conductivity.[5] By plotting time logarithmically (**Figure S2D**), distinct stages of sintering can be qualitatively observed. Quantitative treatment of densification kinetics of cold sintered materials lies outside the scope of the present study but are treated in more detail elsewhere.[1], [2]

2. XRD refinements

Rietveld refinements (performed with the software FullProf) were conducted to confirm the phase composition of the starting powder, the as-CSP sample and cold sintered sample annealed at 900 °C and 1200 °C. Quantitative information such as phase fractions, crystallite size were not determined as refinements were conducted on routine and low intensity XRD patterns suitable for phase identification. For the powder (**Figure S3C**), the as-CSP sample (**Figure S3F**) and the cold sintered sample annealed at 900 °C (**Figure S3H**), the most satisfactory Rietveld refinements were obtained in simulating three phases: β''-Al_2O_3 phase (rhombohedral, $R\bar{3}m$), β'-Al_2O_3 phase (hexagonal, $P6_3/mmc$) and Na_2CO_3 (monoclinic, C2/m). For the cold sintered sample annealed at 1200 °C, Rietveld refinements were equivalent with both (ii) $R\bar{3}m$ and $P6_3$/mmc space groups and (iii) $R\bar{3}m$, $P6_3$/mmc and C2/m as shown in **Figure S3I** and **J**, respectively. This implies a negligible presence of sodium carbonate (Na_2CO_3) on the sample surface.

3. Additional electron microscopy of the surface of as-cold-sintered SBA samples

The surfaces of as-cold-sintered SBA pellets were polished to 2400 grit using silicon carbide grit paper and sputtered with ca. 10 nm of iridium. The pellets were then imaged with a scanning electron microscope (FESEM Verios) in backscatter mode (**Figure S4A**), secondary electron mode (**Figure S4B**), and with chemical mapping via electron dispersion spectrometry (**Figure S4C-E**). The backscattered electron images shown that the majority of the sample is chemically homogenous, with no secondary phases segregated at grain boundaries, however, there are significant

areas of the surface with a phase lighter than the matrix (SBA) (**Figure S4A**). These areas, which appear dark under secondary electron illumination (**Figure S4B**), are comprised of sodium (**Figure S4C**), carbon (**Figure S4D**), and oxygen (not shown). This observation, coupled with a notable aluminum deficiency (**Figure S4E**) leads us to conclude that these areas are sodium carbonates formed on the surface of the cold sintered SBA pellets upon interacting with air.

Chemical mapping was also performed on samples imaged using scanning transmission electron microscopy (STEM). The results indicated that the major elements (Al, Na, and O) are present throughout the microstructure including the amorphous regions at the grain boundaries, while there is a slight carbon signal at the grain boundaries as well. Some grain boundaries did not contain this carbon signature. This lends to the conclusion that carbonates are present at some grain boundaries in the as-cold-sintered SBA samples.

4. Lotgering Analysis

To investigate the presence of texturing in the cold sintered sodium beta alumina (SBA) samples, a Lotgering analysis was performed on the powder, as-cold-sintered ceramics, and the annealed samples (900°C and 1200°C). Lotgering analysis is a well-known method of comparing the relative peak heights of specific sets of peaks to the complete reflection profile which allows for comparison between the observed microstructure and an ideally randomized spectra.[6] The Lotgering factor (LF) is calculated as:

$$LF = \frac{P - P_o}{1 - P_o}, P = \frac{\sum I_{00l}}{\sum I_{hkl}}, P_o = \frac{\sum I_{o(00l)}}{\sum I_{o(hkl)}}$$

Where I_{00l} are the peak intensities of the (00l) peaks and I_{hkl} are the peak intensities of all the peaks for a given 2θ range (here being 5° to 40°), and I_o denotes the same values derived from a reference structure (here being PDF 04-014-2164). An LF of 0 indicates a perfectly random orientation whereas a value of 1 indicates that the planes of interest are oriented perfectly parallel to the face of the pellet. The (003), (006), and (0,0,15) peaks are often used to calculate the LF values for SBA samples processed under the influence of applied pressure, sometimes reaching as high as 0.9 for some processing methods.[7]

The overlaid XRD spectra of the cold sintered samples relative to the powder is shown in **Figure S5A-D**. Clearly, the relative peak heights differ substantially between the cold sintered samples and the powder. The

corresponding LF values are given in **Figure S5E**, which vary from 0.55 to 0.67 for even the as-cold-sintered sample. These results indicate a modest amount of texturing in the cold sintered ceramics, likely derived from the applied uniaxial pressure. This is supported by observing preferential alignment of the high-aspect ratio hexagonal grains perpendicular to the direction of the applied pressure, exemplified by an annotated scanning electron microscope image in **Figure S5F** and transmission electron microscopy (**Figure 3**, main body).

5. Impedance fitting and equivalent circuits

The impedance spectra of the cold sintered SBA samples were fit using the ZView software (Scribner Associates). The semicircles of the as-cold-sintered SBA were fit with a resistor in parallel with either a Havriliak-Negami element (HN, **Figure S4A**) or a constant-phase element (CPE, **Figure S4B**). When no semicircle was present, a resistor was placed in series with a CPE (**Figure S4C**). The electrode response was modeled with either CPE (**Figure S4A, Figure S4C**) or an open-circuit Warburg element (**Figure S4B**). The open-circuit Warburg element (W_o) captures a finite-diffusion length phenomena associated with the transition from a diffusive to capacitive transition at low frequencies. Inductance is fit with an inductor (L). The equations for each major element used are given below:

$$Z_{CPE} = \frac{1}{T * (j * \omega)^P}$$

$$Z_{R//CPE} = \frac{R}{T * (j * \omega)^P}$$

$$Z_{HN} = \frac{R}{\left(1 + [j * T * \omega]^U\right)^P}$$

$$W_o = R * \frac{coth\left[(j * T * \omega)^P\right]}{(j * T * \omega)^P}$$

Where R is the resistance, j is $\sqrt{-1}$, ω is the angular frequency ($\omega = 2\pi * f$), where f is the frequency, and T, P, and U are adjustable fitting parameters.

6. Extraction of data from the literature

In order to place cold sintering within the context of previous studies regarding the processing of β''-Al_2O_3, a representative set of data (density and ionic conductivity) from the literature was extracted and plotted against that

of cold sintered β''-Al_2O_3 both as a function of measurement temperature and sintering temperature (**Figure S8**, **Table S3**). For comparability, preference was given to studies which used Mg-doped β''-Al_2O_3. For studies which report properties which respect to the axis of pressure applied during sintering, preference was given to data collected parallel to the pressing direction since this most comparable to the data reported in this work. Precise data values were used when they were available in the referenced texts. Otherwise, the data was extracted manually from the relevant figures using the *WebplotDigitizer* program.[8] Owing to the manual extraction process, there is likely a small of amount of error in the values but this should not affect the qualitive comparisons made in the manuscript. Values from **Figure 9** (main body) are collated in **Table S4**.

6. Electronic Supporting Information Figures

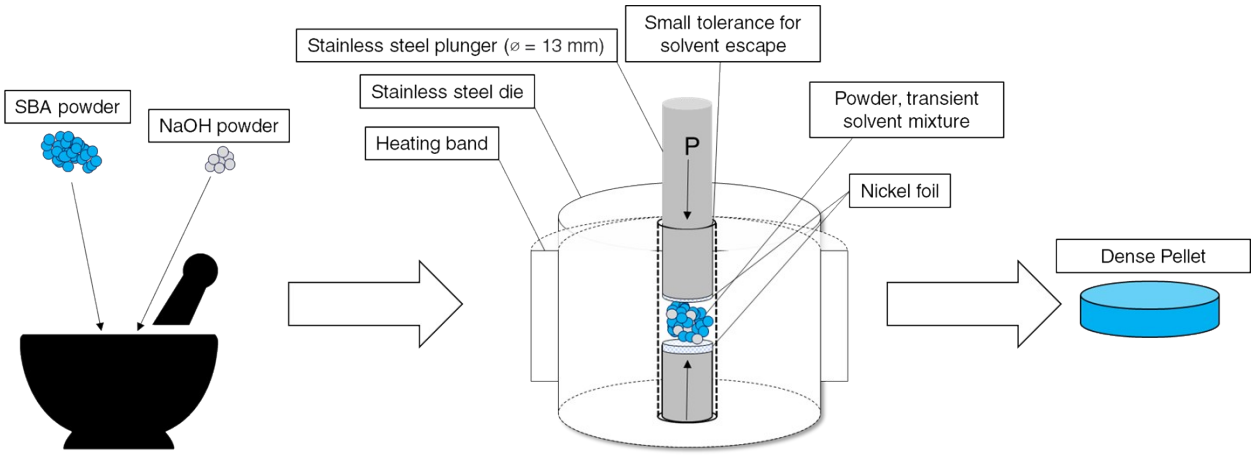

Figure S1 A schematic of the cold sintering process. The SBA powder and solid NaOH powder are mechanically mixed in a mortar and pestle. This is followed by the introduction of the powder mixture into a stainless-steel die, which is wrapped in a heating band. Uniaxial pressure is applied to cylindrical plungers via a carver press. The platens of the press (not shown) are heated approximately 275°C to reduce thermal losses. After cold sintering is complete, a disk-shaped pellet is ejected from the die.

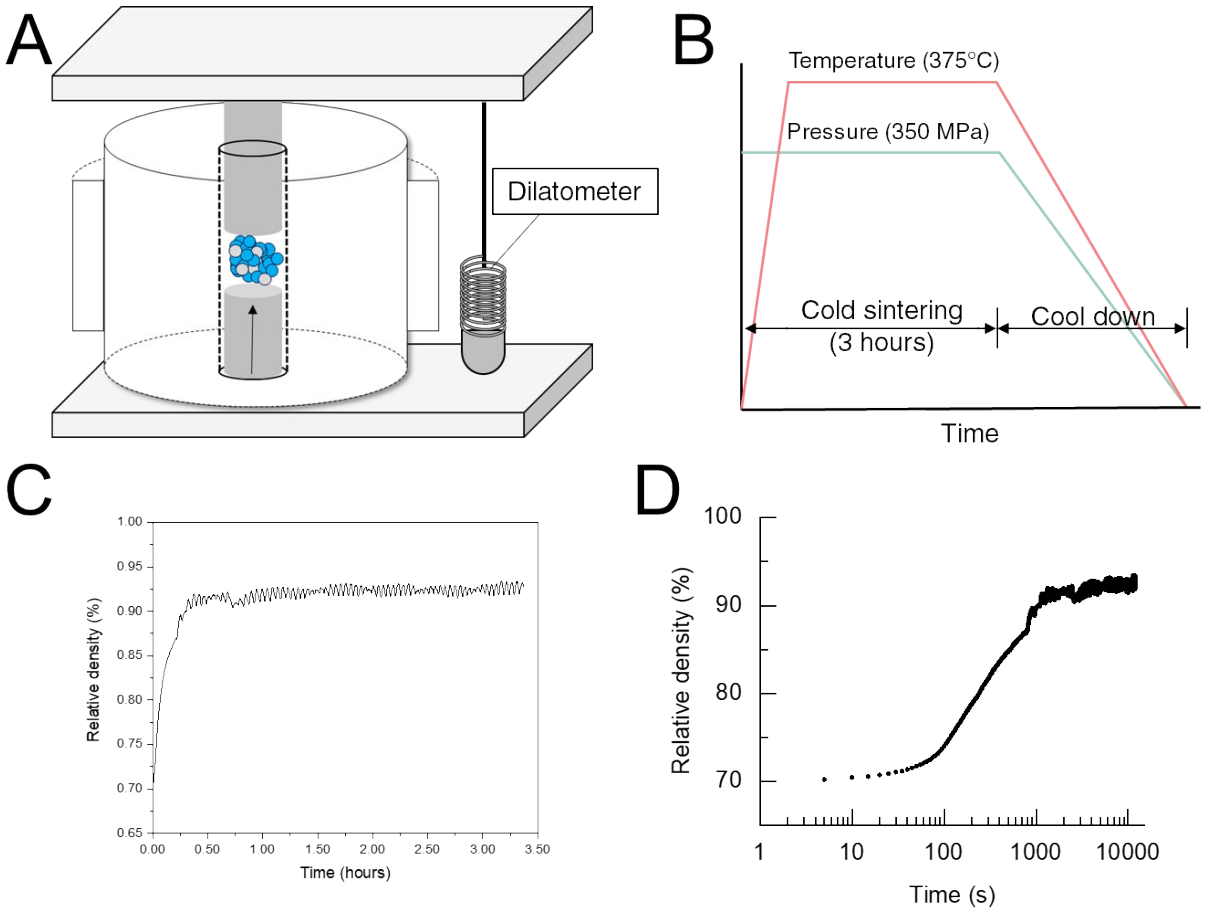

Figure S2 The cold sintering process can be monitored *in-situ* by the addition of a dilatometer which measures the linear shrinkage of the press during sintering (**A**). The approximate temperature-pressure profile of the process is given in (**B**). The relative density as a function of time is calculated by relating the final density of the pellet to the linear shrinkage measured by the dilatometer. The absolute density as a function of time for an SBA pellet densified with a eutectic mixture of NaOH/KOH at 200°C is shown in (**C**), while the distinct stages of densification can be observed by plotting time on a logarithmic scale (**D**). The final density of the pellet is 93%.

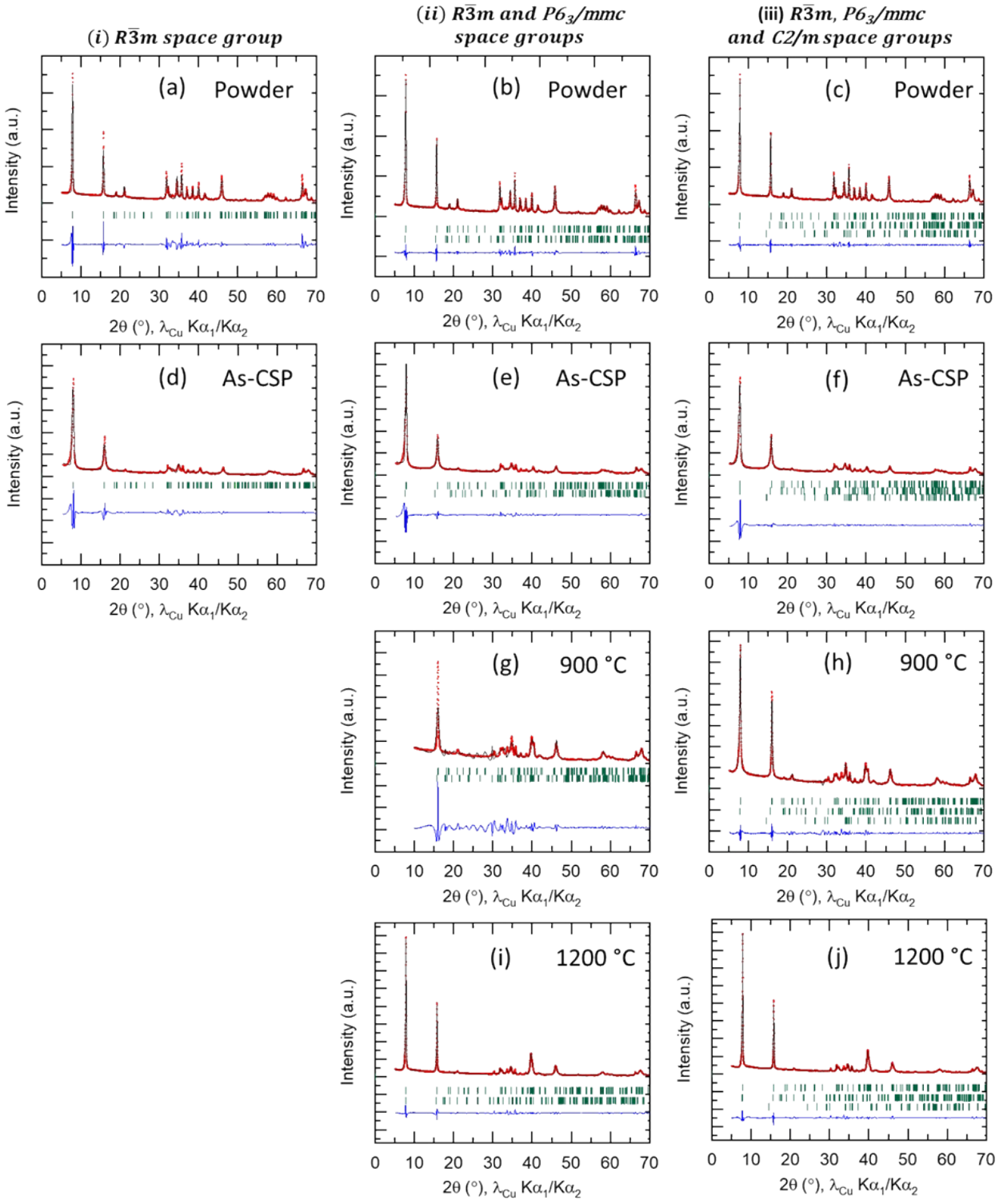

Figure S3 XRD patterns of β-Al_2O_3 refined with: (i) the $R\bar{3}m$ space group – Rhombohedral phase for the (**A**) powder, (**D**) as-cold sintered sample; (ii) $R\bar{3}m$ and $P6_3/mmc$ (hexagonal phase) space groups for the (**B**) powder, (**E**) as-cold

sintered sample, (**G**) cold sintered sample annealed at 900 °C (**I**) cold sintered sample annealed at 1200 °C; (iii) R $\bar{3}m$, $P6_3/mmc$ and C2/m (monoclinic phase for Na_2CO_3) space groups for the (**C**) powder, (**F**) as-cold sintered sample, (**H**) cold sintered sample annealed at 900 °C (**J**) cold sintered sample annealed at 1200 °C. The continuous black line, the red crosses, and the bottom blue line represent the calculated, observed and difference patterns, respectively. The green vertical ticks represent Bragg positions of diffraction peaks in β-Al_2O_3.

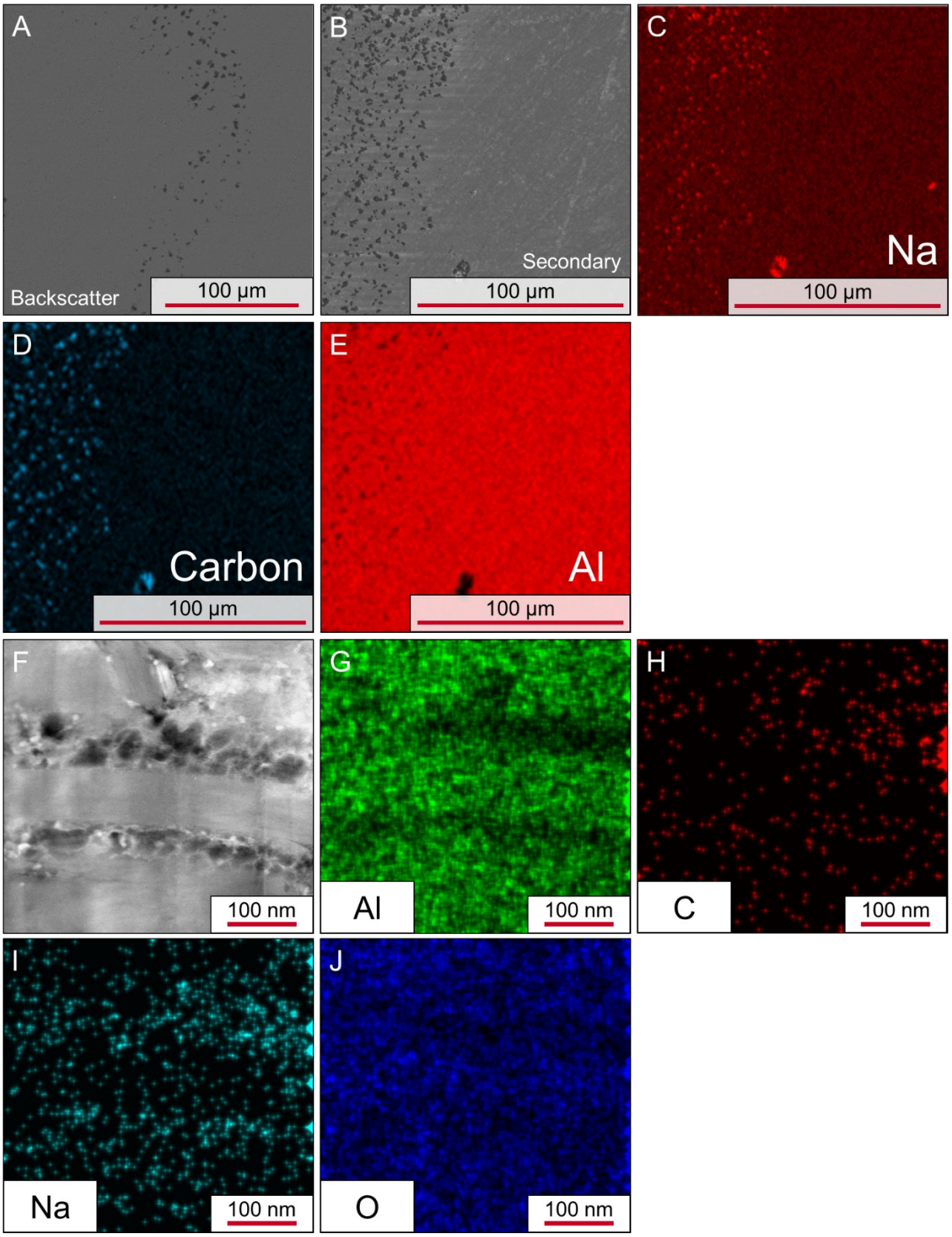
A
Backscatter
100 µm
B
Secondary
100 µm
C
Na
100 µm
D
Carbon
100 µm
E
Al
100 µm
F
100 nm
G
Al
100 nm
H
C
100 nm
I
Na
100 nm
J
O
100 nm

Figure S4 Polished surface of a cold sintered SBA sample in backscatter mode (**A**), secondary electron mode (**B**), and with chemical mappings (**C-E**). STEM image of as-cold-sintered SBA with associated chemical mapping via EDS (**F-J**).

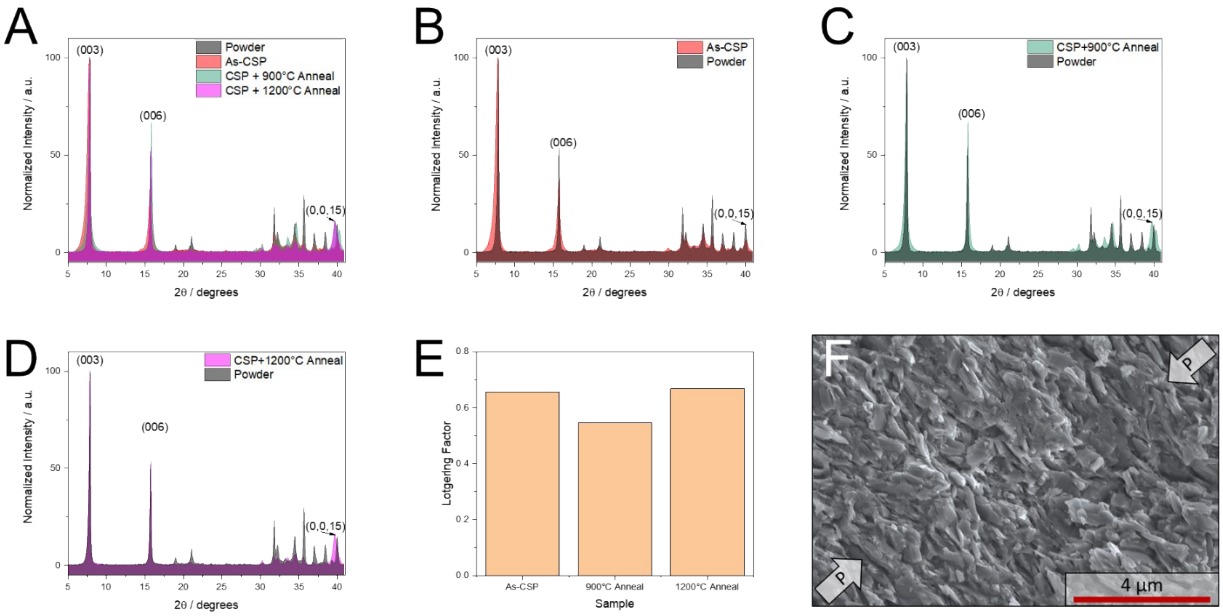

Figure S5 XRD spectra of the SBA powder and cold sintered samples normalized to the (003) peak heigh (**A**) and individual couples of the powder with each sample (**B-D**). The calculated Lotgering factors of the cold-sintered samples (**E**). An SEM image of an as-cold-sintered SBA sample with a significant portion of the grains oriented perpendicular to the direction of applied pressure, denoted by arrows with an inscribed "*P*" (**F**).

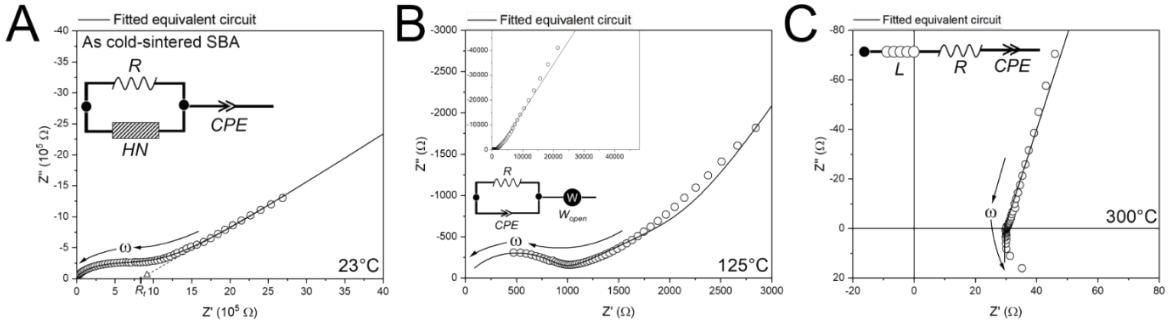

Figure S6 Room temperature EIS spectra for as-cold-sintered SBA, fitted with inset equivalent circuit using values given in **Table S1**.

Table S1

Figure S6A	**R**	**HN-T**	**HN-P**	**HN-U**	**CPE-T**	**CPE-P**
As-CSP, 23°C	1.19E6	1.28E-6	6.95	0.31	5.86E-7	0.43

Figure S6B	**R**	**CPE-T**	**CPE-P**	**W_o-R**	**W_o-T**	**W_o-P**
As-CSP, 125°C	867.5	1.72E-8	0.72	3443	0.033	0.35

Figure S6C	**L**	**R**	**CPE-T**	**CPE-P**
As-CSP, 300°C	2.17E-6	29.6	5.22E-5	0.84

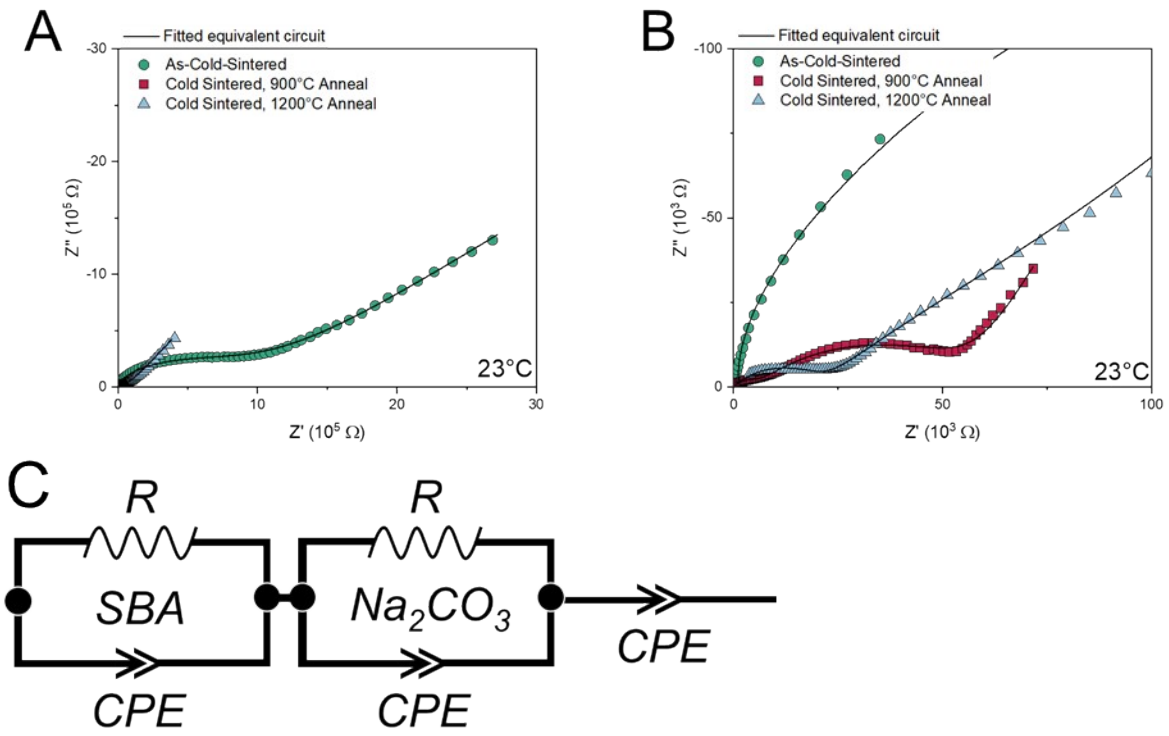

Figure S7 EIS spectra of cold sintered SBA which has been annealed at either 900°C or 1200°C. Fitted with equivalent circuit given in (**C**) using parameters given in Table S2.

Table S2 Fitting parameters for Figure S7.

	SBA			Na_2CO_3			Electrode	
23°C	**R**	**CPE-T**	**CPE-P**	**R**	**CPE-T**	**CPE-P**	**CPE-T**	**CPE-P**
CSP+900°C Anneal	5380	4.45E-8	0.65	54291	1.51E-6	0.74	3.40E-5	0.74
CSP+1200°C Anneal	21528	2.63E-8	0.56	63091	2.469E-6	0.51	2.55E-6	0.60

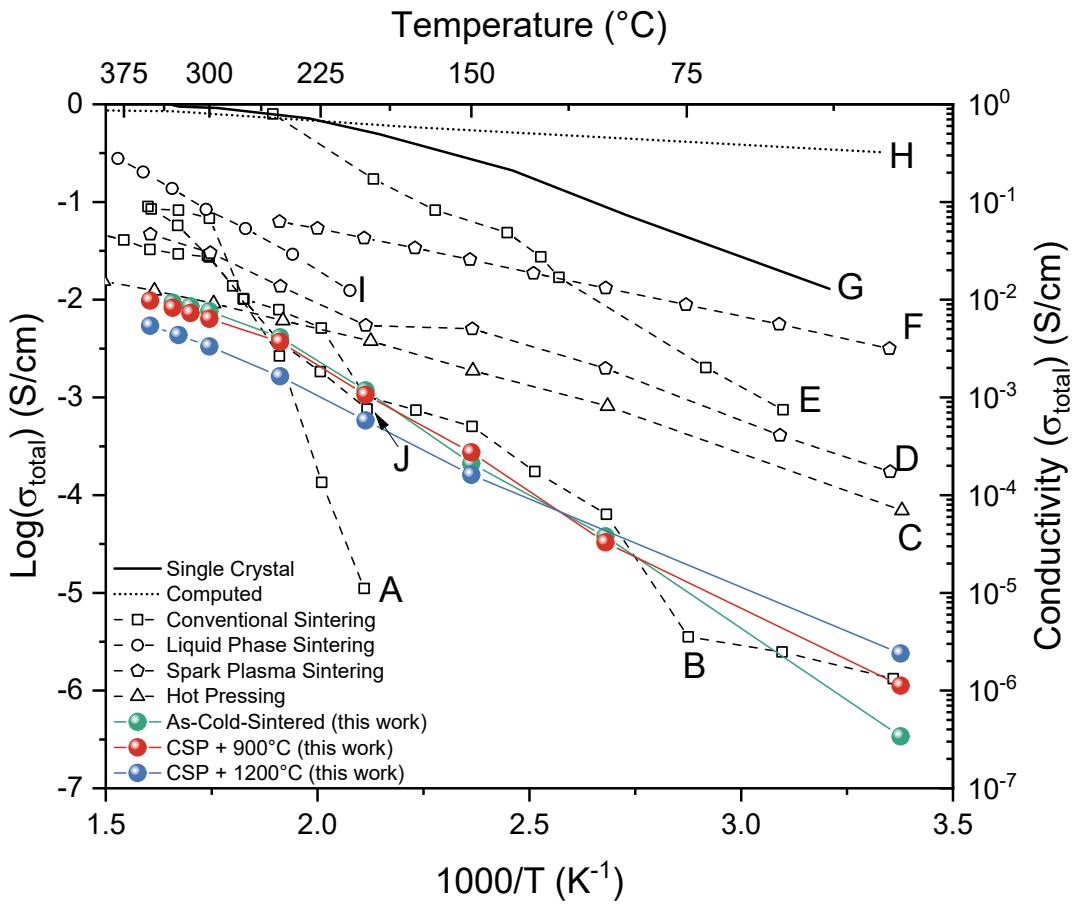

Figure S8 Comparative Arrhenius plot shown in **Figure 5** of the main body, with letter codes to specify referenced study.

Table S3 Legend of references used to compile comparative Arrhenius plot (**Figure S8** and **Figure 5** of the main body).

Letter	Reference	Category
A	[9]	Conventional Sintering
B	[10]	Conventional Sintering
C	[11]	Hot Pressing
D	[12]	Spark Plasma Sintering
E	[13]	Conventional sintering
F	[14]	Spark Plasma Sintering
G	[15]	Single Crystal
H	[15]	Computed
I	[16]	Liquid Phase Sintering (1 mol.% SnO_2)
J	[17]	Conventional sintering

Table S4 Table of the data used to compile the comparative sintering temperature versus conductivity at 300°C and sintering temperature versus relative density plots of the main body (**Figure 9A** and **9B** of the main body, respectively) Abbreviations: CS – Conventional Sintering, HP – Hot Pressing, LPS – Liquid Phase Sintering,

Reference	Category	Sintering Temperature (°C)	Relative Density (%)	σ at 300°C ($S.cm^{-1}$)	Note
[17]	CS	1550	71.7	2.75E-02	
[18]	CS	1800	95	6.65E-02	
[13]	CS	1620	96	1.10E-01	
[10]	CS	1600	98.5	9.10E-02	
[9]	CS	1600	98.5	2.80E-02	

[7]	CS	1620	93.7	-	
[19]	CS	1600	92.2	2.60E-02	
[20]	CS	1650	93	-	
[21]	CS	1580	89.4	3.58E-02	
[22]	CS	1600	92	-	
[16]	CS	1620	96.5	-	
[16]	CS	1570	95.9	-	
[16]	CS	1520	94.3	4.80E-02	
[23]	CS	1700	97	4.37E-02	Interpolated conductivity.
[24]	CS	1585	96.2	1.30E-01	Averaged from set of samples.
[25]	CS	1330	74	-	
[25]	CS	1380	84	-	
[25]	CS	1430	92	-	
[25]	CS	1450	94	-	
[25]	CS	1480	96	-	
[25]	CS	1500	97	-	
[25]	CS	1560	99	1.00E-01	
[26]	CS	1450	95.98	7.52E-03	
[11]	HP	1700	99	9.10E-03	30 MPa, 10% excess Na

[27]	HP	1400	99	2.00E-01	4500 psi (31 MPa)
[28]	HP	1100	91.7	-	a-series, 150 kg cm^{-2}
[28]	HP	1300	98.3	-	a-series, 150 kg cm^{-2}
[28]	HP	1500	99.7	-	a-series, 150 kg cm^{-2}
[28]	HP	1100	94.5	-	c-series, 300 kg cm^{-2}
[28]	HP	1300	95.3	-	c-series, 300 kg cm^{-2}
[28]	HP	1500	100	-	c-series, 300 kg cm^{-2}
[21]	LPS	1580	96.2	1.88E-01	1% TiO_2
[16]	LPS	1620	97	-	0.5% SnO_2
[16]	LPS	1569	96.2	-	0.5% SnO_2
[16]	LPS	1519	94.8	-	0.5% SnO_2
[16]	LPS	1620	99.5	-	1% SnO_2
[16]	LPS	1570	96.2	-	1% SnO_2
[16]	LPS	1520	98.2	8.40E-02	1% SnO_2
[16]	LPS	1620	97.3	-	2% SnO_2
[16]	LPS	1570	96.8	-	2% SnO_2
[16]	LPS	1520	95.2	-	2% SnO_2
[29]	LPS	1400	83	-	SBA/YSZ/TiO_2
[29]	LPS	1500	85.5	-	SBA/YSZ/TiO_2

[29]	LPS	1400	98.3	4.90E-02	SBA/YSZ/TiO_2/MnO_2
[29]	LPS	1500	98.5	4.00E-02	SBA/YSZ/TiO_2/MnO_2
[26]	LPS	1450	98.2	1.37E-02	0.01% NiO
[26]	LPS	1450	98.4	1.28E-02	0.05% NiO
[26]	LPS	1450	98.3	2.16E-02	0.1% NiO
[26]	LPS	1450	98.6	2.51E-02	0.15% NiO
[26]	LPS	1450	98.7	3.01E-02	0.25% NiO
[26]	LPS	1450	97.9	1.26E-02	0.5% NiO
[26]	LPS	1450	96.7	9.15E-03	1.0% NiO
[26]	LPS	1450	92.8	7.46E-03	1.5% NiO
[12]	SPS	1300	96.4	3.00E-02	40 MPa, "flaky", perpendicular to SPS direction
[12]	SPS	1300	96.4	9.00E-02	40 MPa, "flaky", parallel to SPS direction.
[7]	SPS	1400	98.9	6.30E-02	Highest conductivity measurement at 250°C.
[30]	SPS	1450	78	-	Conductivity only measured at 550°C
[30]	SPS	1450	88	-	Conductivity only measured at 550°C

[31]	VPS	1700	97	6.80E-02	Perpendicular to texture direction
[31]	VPS	1500	99	2.60E-02	Perpendicular to texture direction
[32]	VPS	1600	97.6	1.70E-02	40% YSZ
[33]	VPS	1500	98.6	5.37E-02	0.4% MgO
[33]	VPS	1500	95.4	2.46E-02	1.6% MgO
This work	Cold Sintering	375	92.7	7.60E-03	
This work	Cold Sintering + Anneal	900	89.6	6.40E-03	
This work	Cold Sintering + Anneal	1200	83.8	3.20E-03	

References

[1] S. H. Bang, A. Ndayishimiye, and C. A. Randall, "Anisothermal densification kinetics of cold sintering process below 150°C," *J. Mater. Chem. C*, 2020.

[2] R. Floyd, S. Lowum, and J.-P. Maria, "Instrumentation for automated and quantitative low temperature compaction and sintering," *Rev. Sci. Instrum.*, vol. 90, no. 5, 2019.

[3] K. Tsuji *et al.*, "Single Step Densification of High Permittivity BaTiO3 at 300 °C," *J. Eur. Ceram. Soc.*, 2019.

[4] S. Lowum, R. Floyd, and J.-P. Maria, "Hydroflux-assisted densification: applying flux

crystal growth techniques to cold sintering," *J. Mater. Sci.*, 2020.

[5] M. Meyer, V. Jaenisch, P. Maass, and A. Bunde, "Mixed alkali effect in crystals of β− and β"-alumina structure," *Phys. Rev. Lett.*, vol. 76, no. 13, pp. 2338–2341, 1996.

[6] R. Furushima, S. Tanaka, Z. Kato, and K. Uematsu, "Orientation distribution-Lotgering factor relationship in a polycrystalline material - As an example of bismuth titanate prepared by a magnetic field," *J. Ceram. Soc. Japan*, vol. 118, no. 1382, pp. 921–926, 2010.

[7] K. Koganei, T. Oyama, M. Inada, N. Enomoto, and K. Hayashi, "C-axis oriented β″-alumina ceramics with anisotropic ionic conductivity prepared by spark plasma sintering," *Solid State Ionics*, vol. 267, pp. 22–26, 2014.

[8] A. Rohatgi, "WebPlotDigitizer." Pacifica, California, USA, 2020.

[9] S. T. Lee, D. H. Lee, J. S. Kim, and S. K. Lim, "Influence of Fe and Ti addition on properties of Na+-β/β″-alumina solid electrolytes," *Met. Mater. Int.*, vol. 23, no. 2, pp. 246–253, 2017.

[10] S. T. Lee, D. H. Lee, S. M. Lee, S. S. Han, S. H. Lee, and S. K. Lim, "Effects of calcium impurity on phase relationship, ionic conductivity and microstructure of Na+-β/β″-alumina solid electrolyte," *Bull. Mater. Sci.*, vol. 39, no. 3, pp. 729–735, 2016.

[11] A. Kishimoto, K. Shimokawa, and S. J. Jung, "Effect of sodium content on the mechanical and electrical properties of preferentially oriented Naβ-alumina ceramics," *J. Mater. Sci. Lett.*, vol. 22, no. 15, pp. 1083–1085, 2003.

[12] K. Li, Y. Yang, X. Zhang, and S. Liang, "Highly oriented β″-alumina ceramics with

excellent ionic conductivity and mechanical performance obtained by spark plasma sintering technique," *J. Mater. Sci.*, vol. 55, no. 20, pp. 8435–8443, 2020.

[13] Y. Sheng, P. Sarkar, and P. S. Nicholson, "The mechanical and electrical properties of ZrO2-Na β″-Al2O3 composites," *J. Mater. Sci.*, vol. 23, no. 3, pp. 958–967, 1988.

[14] K. Koganei, T. Oyama, M. Inada, N. Enomoto, and K. Hayashi, "C -axis oriented β ″ -alumina ceramics with anisotropic ionic conductivity prepared by spark plasma sintering," *Solid State Ionics*, vol. 267, pp. 22–26, 2014.

[15] B. Wang and A. N. Cormack, "Molecular dynamics simulations of Mg-doped beta″-alumina with potential models fitted for accurate structural response to thermal vibrations," *Solid State Ionics*, vol. 263, pp. 9–14, 2014.

[16] H. A. Moghadam and M. H. Paydar, "Low-temperature sintering of sodium beta alumina ceramics using nanosized SnO2 sintering aid," *Process. Appl. Ceram.*, vol. 14, no. 1, pp. 56–62, 2020.

[17] S. Barison, S. Fasolin, C. Mortalò, S. Boldrini, and M. Fabrizio, "Effect of precursors on β-alumina electrolyte preparation," *J. Eur. Ceram. Soc.*, vol. 35, no. 7, pp. 2099–2107, 2015.

[18] A. Hooper, "A study of the electrical properties of single-crystal and polycrystalline β-alumina using complex plane analysis," *J. Phys. D. Appl. Phys.*, vol. 10, no. 11, pp. 1487–1496, 1977.

[19] S. J. Shan, L. P. Yang, X. M. Liu, X. L. Wei, H. Yang, and X. D. Shen, "Preparation and characterization of TiO2 doped and MgO stabilized Na-β″-Al2O3 electrolyte via a citrate

sol-gel method," *J. Alloys Compd.*, vol. 563, pp. 176–179, 2013.

[20] A. Mali and A. Petric, "Synthesis of sodium β'-alumina powder by sol-gel combustion," *J. Eur. Ceram. Soc.*, vol. 32, no. 6, pp. 1229–1234, 2012.

[21] X. Wei, Y. Cao, L. Lu, H. Yang, and X. Shen, "Synthesis and characterization of titanium doped sodium beta″-alumina," *J. Alloys Compd.*, vol. 509, no. 21, pp. 6222–6226, 2011.

[22] A. C. Sutorik, S. S. Neo, D. R. Treadwell, and R. M. Laine, "Synthesis of ultrafine β″-alumina powders via flame spray pyrolysis of polymeric precursors," *J. Am. Ceram. Soc.*, vol. 81, no. 6, pp. 1477–1486, 1998.

[23] A. Imai and M. Harata, "Ionic conduction of impurity-doped β-alumina ceramics," *Jpn. J. Appl. Phys.*, vol. 11, no. 2, pp. 180–185, 1972.

[24] T. J. Whalen, G. J. Tennenhouse, and C. Meyer, "Relation of Properties to Microstructure in a B"-Alumina Ceramic," *J. Am. Ceram. Soc.*, vol. 57, pp. 497–498, 1974.

[25] H. Li *et al.*, "Performance of Nano-3YSZ toughened β''-Alumina solid electrolyte prepared by EDTA-Zr(IV)/Y(III) complex as surface modifier," *J. Alloys Compd.*, vol. 817, p. 152717, 2020.

[26] C. Zhu, Y. Hong, and P. Huang, "Synthesis and characterization of NiO doped beta-Al2O3solid electrolyte," *J. Alloys Compd.*, vol. 688, pp. 746–751, 2016.

[27] A. V. Virkar, G. J. Tennenhouse, and R. S. Gordon, "Hot Pressing of Li2O-Stabilized Beta''-Alumina," *J. Am. Ceram. Soc.*, vol. 57, no. 11, p. 508, 1974.

[28] P. Vincenzini, A. Bellosi, and G. N. Babini, "The Influence of Powder Characteristics on the Vacuum Hot Pressing of Sodium Beta-Aluminas," *Mater. Chem.*, vol. 3, pp. 129–156,

1978.

[29] X. Lu, G. Li, J. Y. Kim, K. D. Meinhardt, and V. L. Sprenkle, “Enhanced sintering of b 00-Al 2 O 3 /YSZ with the sintering aids of TiO 2 and MnO 2.”

[30] L. B. Caliman, R. Bouchet, D. Gouvea, P. Soudant, and M. C. Steil, “Flash sintering of ionic conductors: The need of a reversible electrochemical reaction,” *J. Eur. Ceram. Soc.*, vol. 36, no. 5, pp. 1253–1260, 2016.

[31] T. D. Sparks and L. Ghadbeigi, “Anisotropic properties of Na-β″-alumina + YSZ composite synthesized by vapor phase method,” *J. Mater. Res.*, vol. 33, no. 1, pp. 81–89, 2018.

[32] S. C. Ligon, G. Blugan, M. C. Bay, C. Battaglia, M. V. F. Heinz, and T. Graule, “Performance analysis of Na-β″-Al2O3/YSZ solid electrolytes produced by conventional sintering and by vapor conversion of α-Al2O3/YSZ,” *Solid State Ionics*, vol. 345, no. June 2019, p. 115169, 2020.

[33] C. Zhang, L. Zhang, P. Zheng, and X. Zhang, “Synthesis of magnesium-beta-alumina composite electrolytes via a vapour phase method,” *Ceram. Int.*, vol. 46, no. 8, pp. 12232–12237, 2020.